ELSEVIER

Physica A 233 (1996) 587–605

PHYSICA A

Pattern formation in sedimentary rocks: Connectivity, permeability, and spatial correlations

Hernán A. Makse[a], Shlomo Havlin[a,b], Plamen Ch. Ivanov[a], Peter R. King[c], Sona Prakash[a], H. Eugene Stanley[a,*]

[a] *Center for Polymer Studies and Department of Physics, Boston University, Boston, MA 02215, USA*
[b] *Department of Physics, Bar-Ilan University, Ramat Gan, Israel*
[c] *BP Exploration Operating Company Ltd., Sunbury-on-Thames, Middx., TW16 7LN, UK*

Abstract

Sedimentary rocks have complicated permeability patterns arising from the geological processes that formed them. We concentrate on pattern formation in one particular geological process, avalanches (grain flow) in wind-blown or fluvial sands. We present a simple experiment and numerical model of how these avalanches cause segregation in particle size that lead to characteristic laminated patterns. We also address the longstanding question of how such patterns are generated. We analyze data on two sandstone samples from different, but similar, geological environments, and find that the permeability fluctuations display long-range power-law correlations characterized by an exponent H. For both samples, we find $H \approx 0.82$–0.90. These permeability fluctuations significantly affect the flow of fluids through the rocks. We demonstrate this by investigating the influence of long-range correlation on percolation properties, like cluster morphology. We relate these properties to characteristics important for hydrocarbon recovery such as breakthrough time for injected fluids and recovery efficiency.

1. Introduction

Sedimentary rocks have complex correlated patterns that influence the flow and recovery of hydrocarbons. These patterns arise from the complicated geological processes that formed the rocks. It is a major experimental and theoretical challenge to understand how the process forms the patterns. For oil companies it is also extremely important to understand how the patterns influence recovery and to make quantitative predictions of the influence.

* Corresponding author. Tel.: +1-617-3532617; fax: +1-617-3533783; e-mail: hes@buphyk.bu.edu.

PII S0378-4371(96)00246-4

In this paper we address the following points:

(i) The formation of periodic laminae of fine and coarse grains in sedimentary structures is a widespread phenomenon [1–8], its origin remains an open question. Fig. 1(a) shows a section of a Triassic, planar cross-bedded Aeolian sandstone from Lochabriggs near Dumfries, Scotland where a typical example of stratification pattern is observed. We address the longstanding question of how such periodic patterns are generated by proposing a "table top" experiment [9]. The experiment reproduces the successive layers of fine and coarse particles observed in sedimentary structures.

(ii) We confirm the spatial patterns predicted with the experiment by comparing with real rock samples. Fig. 2(a) shows the result of the experiment [9]. The size segregation into alternating layers is quite similar to that found in the geological sample and in stratigraphic records. We note two features:
   (a) *Alternation.* We clearly see the formation of alternating layers consisting of small and large particles.
   (b) *Segregation.* We observe that the layers are built up in such a way that small particles are segregated in layers near the top of the slip-face, while larger particles form layers near the substrate at the bottom.

(iii) We propose a physical explanation of the process involved. A numerical computer model of sand dune dynamics is developed that confirms the plausibility of the physical mechanism [9] (Fig. 2(b)).

(iv) We quantify the spatial correlations in rocks. Permeability in sandstone can change by many orders of magnitude over very short distances. Not only are there large fluctuations in permeability but the permeability can exhibit strong anisotropy. Deriving methods to describe these spatial patterns is a major challenge. Both the efficient recovery of hydrocarbon and contaminant dispersal and control in ground water is affected by the understanding of such spatial patterns. Traditionally, these patterns have been modeled with a finite range correlation scale. We analyze a detailed permeability map and show that the data are consistent with a long-range correlation model [14].

2. Rock slab data

The Aeolian sandstone shown in Fig. 1(a) was formed by wind-blown sand [1]. A small sand accumulation (sand bar or dune) is formed as the unidirectional wind moves material along the bed. As the wind continues, sand is moved from the upstream side of the dune to the crest of the dune, and the slope of the sand bar becomes steeper. When the initial dune reaches a critical angle or slope, a downstream slip-face is developed where avalanches of sand begins. After this, new material is brought to the top of the dune until another avalanche occurs. The evidence of such sedimentary process can be traced in the layered structure of the Lochabriggs sample of Fig. 1(a).

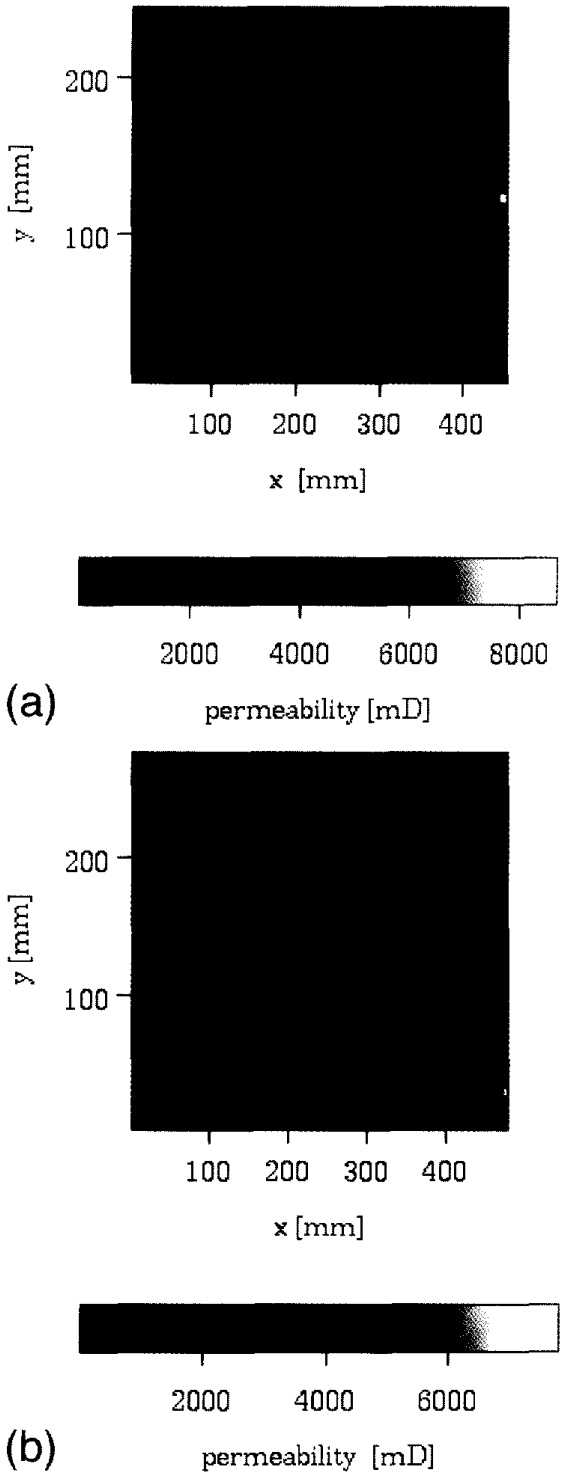

Fig. 1. (a) Permeability map of the Lochabriggs sample. The complete sample consists of two slabs of 448 mm by 246 mm and 10 mm thick, and again only three faces were used in this study. The permeability was measured every 12 and 4 mm in the x and y directions, respectively, so that a grid of $n_x = 38$ by $n_y = 61$ was obtained. Notice the strong anisotropy of this sample manifested by the crests elongated along the y' direction. (b) Permeability map of the Hollington sample. The complete sample consist of two slabs, measuring 474 mm by 276 mm and 10 mm thick. Three faces at heights $z = 0$, $z = 10$, and $z = 20$ mm were used to study the permeability pattern (the $z = 0$ face is shown in this figure). Unfortunately, the measurements of one face were corrupted by instrumentation error and so only three faces could be used. The permeability was measured every 10 mm in the x direction and every 4 mm in the y direction, so a grid of $n_x = 48$ by $n_y = 69$ permeability values was obtained.

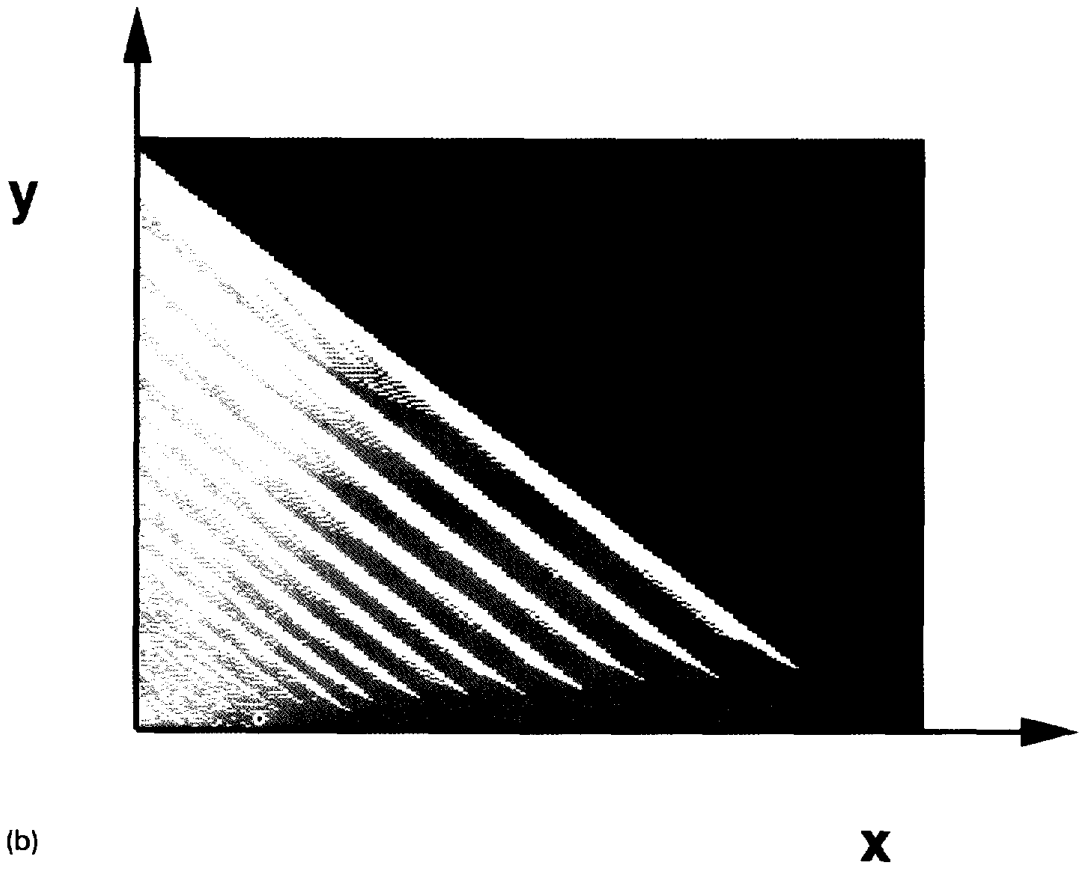

Fig. 2. (a) Photograph of the experimental sandpile showing the periodic layers. (b) Image obtained with the proposed sandpile model.

3. Experiment

To understand the origin of the layering segregation we begin by developing the following "table-top" experiment [9]. The experimental setup consists of a vertical Hele-Shaw [10] cell with a gap of 5 mm separating two transparent plates of 300 mm by 200 mm (see Fig. 2(a)). We close the left edge of the cell leaving the right edge free, and we pour, next to the left edge, an equal-volume mixture of white fine silica sand (typical size 0.4 mm) and dark coarse sugar crystals (typical size 0.9 mm). We choose this quasi-two-dimensional geometry since the actual geological system is translationally invariant along the transverse direction (due to the unidirectional flow of sand).

Fig. 2(a) shows the result of the experiment. We note the two main features: (a) alternation, and (b) segregation.

4. Process model and numerical computer model

The main physical mechanism responsible for the formation of the layers appears to be related to the segregation effect and also to the existence of two critical angles controlling the avalanche process [9]. Indeed, real sandpiles are known [11–13] to be stable until the angle of the sandpile θ reaches a critical maximum angle of stability θ_m. When $\theta > \theta_m$, the sandpile produces a spontaneous avalanche. The avalanche stops when θ decreases below a second critical angle of repose θ_r. The oscillation of θ between θ_m and θ_r as sand is continually added produces the periodic layers observed in the experiment, and presumably in geological data as well.

We next develop a mean field numerical sandpile model [9], defined in a semi-infinite $(1+1)$-dimensional lattice corresponding to the experimental setup. Particles are chosen one at a time. They are selected at random to be either small or large. Each particle is released near the left edge of the semi-infinite lattice. If the local angle it makes exceeds a critical angle of stability θ_m, it is moved one place to the right, and this process is continued until it makes a stable angle or it reaches the substrate. Then the other particles are moved (successively one to the right) until the entire pile is stable – i.e., all angles are below the repose angle θ_r. The deposition now starts again, and the above process is iterated until a large sandpile of typically 10^5 particles has been formed.

Fig. 2(b) shows the resulting morphology of the model. Different colors represent different particle size, being white for the smaller particles and dark for the larger particles. The size segregation into alternating layers is quite similar to that found experimentally (Fig. 2(a)), which in turn is reminiscent of the stratification structure of the geological Lochabriggs sample (Fig. 1(a)).

5. Spatial correlations and connectivity

Next we discuss spatial patterns in permeable rocks. We analyzed two samples: one the *aeolian* Lochabriggs (Lo) sample shown in Fig. 1(a), and the second sample

a Triassic, *fluvial* trough cross-bedded sandstone from Hollington (Ho) near Stafford in the East Midlands of England (Fig. 1(b)) [14]. The deposition process is similar. Now the grains are deposited under water. Eddying on the slip face of the sand bar influences the avalanching slightly.

Permeability on the small scale of both rock samples was measured by standard mini-permeametry [14,15]. The mini-permeameter is a tube through which a gas (air in laboratory measurements) is blown into the rock sample at a fixed pressure. The flow rate of the gas into the rock sample is measured. The permeability k is then the ratio of the flow rate Q to the pressure drop ΔP (which is applied pressure minus atmospheric pressure) multiplied by the viscosity of the gas μ.

$$k \equiv -\frac{\mu Q}{\Delta P}\,. \tag{1}$$

Corrections must be made for the compressibility of the gas and the flow geometry, which is hemispherical from the injection point. The end of the permeameter in contact with the rock is made of a flexible plastic ring to ensure a good seal. The probe comes in a variety of sizes to measure permeability fluctuations on different length scales; for our measurements the probe had a 1 cm diameter.

The permeability maps so obtained are shown in Figs. 1(a) and 1(b). By inspection, we see that local permeability varies significantly within a very short length scale, suggesting that the permeability may not be an independent random process.

We plot the permeability histograms for the Sample Ho in Fig. 3. The high permeability zone has a typical permeability of 3300 mD, the low permeability zone has a typical permeability of 30 mD. Local permeability is proportional to the square of the grain radius for uncompacted, well-sorted, clean, quartzite sandstone. The high permeability zone consists of interbedded fine and coarse grain material and hence has a much higher variability. The low permeability zone is more homogeneous, consisting of more exclusively fine grained material.

Next we measure the spatial correlations in permeability. We study the correlations of the permeability field $k(i,j)$ $(i,j = 1,\ldots,n_x,n_y)$ along the x and y directions (see Fig. 1). To this end, we first integrate the permeability variables along both directions separately, by calculating the "net displacements" $x_j(\ell)$ and $y_i(\ell)$:

$$x_j(\ell) \equiv \sum_{i=1}^{\ell} (k(i,j) - \overline{k(j)}) \qquad (j = 1,\ldots,n_y)\,, \tag{2}$$

and

$$y_i(\ell) \equiv \sum_{j=1}^{\ell} (k(i,j) - \overline{k(i)}) \qquad (i = 1,\ldots,n_x)\,, \tag{3}$$

where $\overline{k(j)} = (1/n_x)\sum_{i=1}^{n_x} k(i,j)$ and $\overline{k(i)} = (1/n_y)\sum_{j=1}^{n_y} k(i,j)$ [16]. Then we calculate the variance $V_x(\ell) \equiv \langle \overline{x(\ell)^2} - \overline{x(\ell)}^2 \rangle^{1/2}$ and $V_y(\ell) \equiv \langle \overline{y(\ell)^2} - \overline{y(\ell)}^2 \rangle^{1/2}$ as a function of the lag ℓ [16]. The scaling behavior of the variance

$$V_x(\ell) \sim \ell^{H_x}, \qquad V_y(\ell) \sim \ell^{H_y} \tag{4}$$

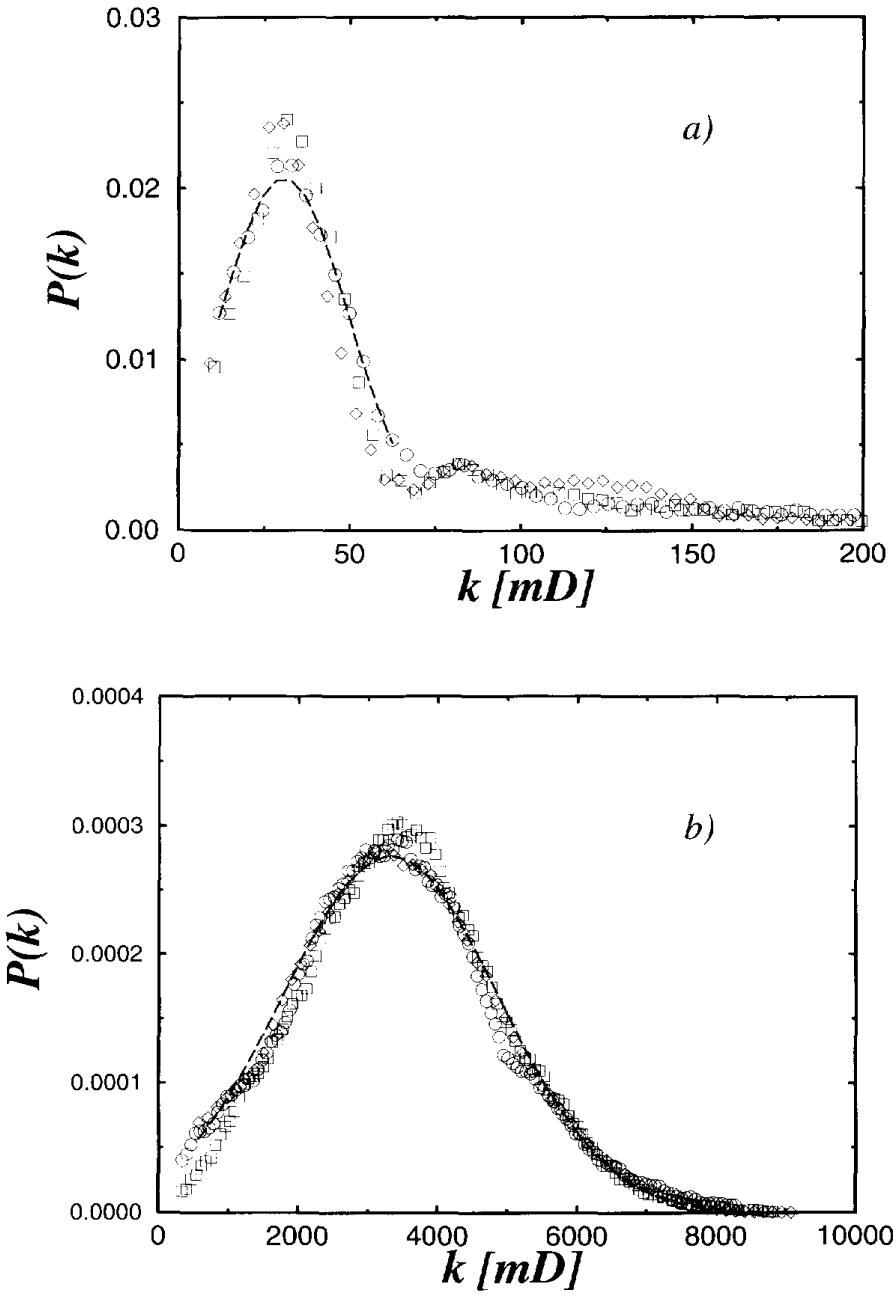

Fig. 3. Normalized permeability distributions for the Sample Ho corresponding to (a) low permeability zone, and (b) high permeability zone. In both figures we plot the distributions corresponding to three different faces of the sample. The distributions are fitted by Gaussian functions. We notice the large difference in the mean value of the permeability between the low and high permeability zones.

can distinguish between short- and long-range correlations. For uncorrelated permeability variables, $H = \frac{1}{2}$, while $\frac{1}{2} < H < 1$ implies persistent long-range correlations among the variables. The correlation exponent H describes the "roughness of the permeability landscape" [17,18].

The method described so far is called r.m.s. fluctuation analysis which however, is known to fail if (i) the signal is nonstationary [19], or (ii) the signal is highly

correlated $H \simeq 1$ [20]. In case (i), the r.m.s. method detects spurious correlations due to the patchiness of the signal [19], while in case (ii) the r.m.s. method gives smaller effective exponents (in particular when small samples are used) because the variance has an upper bound $V(\ell) < \ell$ and therefore the method cannot detect fluctuations with exponent $H \geqslant 1$ [20]. In our case we find that, apart from possible nonstationarities, the permeability values are strongly correlated.

To overcome the limitations of the r.m.s. method, we will analyze the spatial correlations of the permeability by using detrended fluctuation analysis (DFA) [19] and wavelet analysis [21]. The DFA method [19] consists of subtracting the local trend (defined as the ordinate of a linear least-squares fit to the permeability values) in each window of size ℓ defined in (5).

The wavelet transform (WT) of a given function $f(x)$ is defined as

$$T_\Psi(x_0, a) \equiv \frac{1}{a} \int_{-\infty}^{\infty} f(x)\ \Psi\left(\frac{x - x_0}{a}\right) dx\,, \tag{5}$$

where Ψ is the analyzing wavelet, x_0 the translation parameter, and a the scale parameter. After performing the WT with a given wavelet, we can determine the values $x_i(a)$ at which T_Ψ has local extrema. The sum of the absolute values of the local extrema raised to the power q exhibits power-law dependence on the scale a,

$$Z(a, q) \equiv \sum_{\{x_i(a)\}} |T_\Psi(x_i(a), a)|^q \sim a^{\tau(q)}\,, \tag{6}$$

defining the exponent $\tau(q)$.

The function $Z(a,q)$ is directly related to the scaling properties of the qth moment of the signal $f(x)$. For certain values of q, the exponents $\tau(q)$ have known meaning. In particular, $\tau(2)$ is related to the scaling exponent of the Fourier power spectra: $S(f) \sim f^{-\beta}$ with $\beta = 2 + \tau(2)$, and therefore

$$\tau(2) = 2H - 1\,. \tag{7}$$

Thus, $\tau(2) > 0$ indicates the presence of long-range correlations ($H > \frac{1}{2}$), and $\tau(2) = 0$ ($H = \frac{1}{2}$) indicate the absence of correlations. The wavelet method is free from restrictions related to nonstationarities and to the presence of large correlations [21].

The results for the permeability correlations for the Sample Ho are shown in Fig. 4. In Fig. 4(a), we show the correlations for both high and low permeability zones, measured in the x and y directions. In this case, before calculating the variance, the permeability is normalized by dividing by the standard deviation calculated independently for each direction. The data are consistent with power-law correlations; using the DFA method, we find

$$H_x = 0.89 \pm 0.06, \qquad H_y = 0.90 \pm 0.06 \qquad \text{(Ho: DFA)}\,. \tag{8}$$

Results for the correlations along the x direction are shown separately for the high and low permeability zones in Fig. 4(b). The correlations are satisfactorily modeled by a

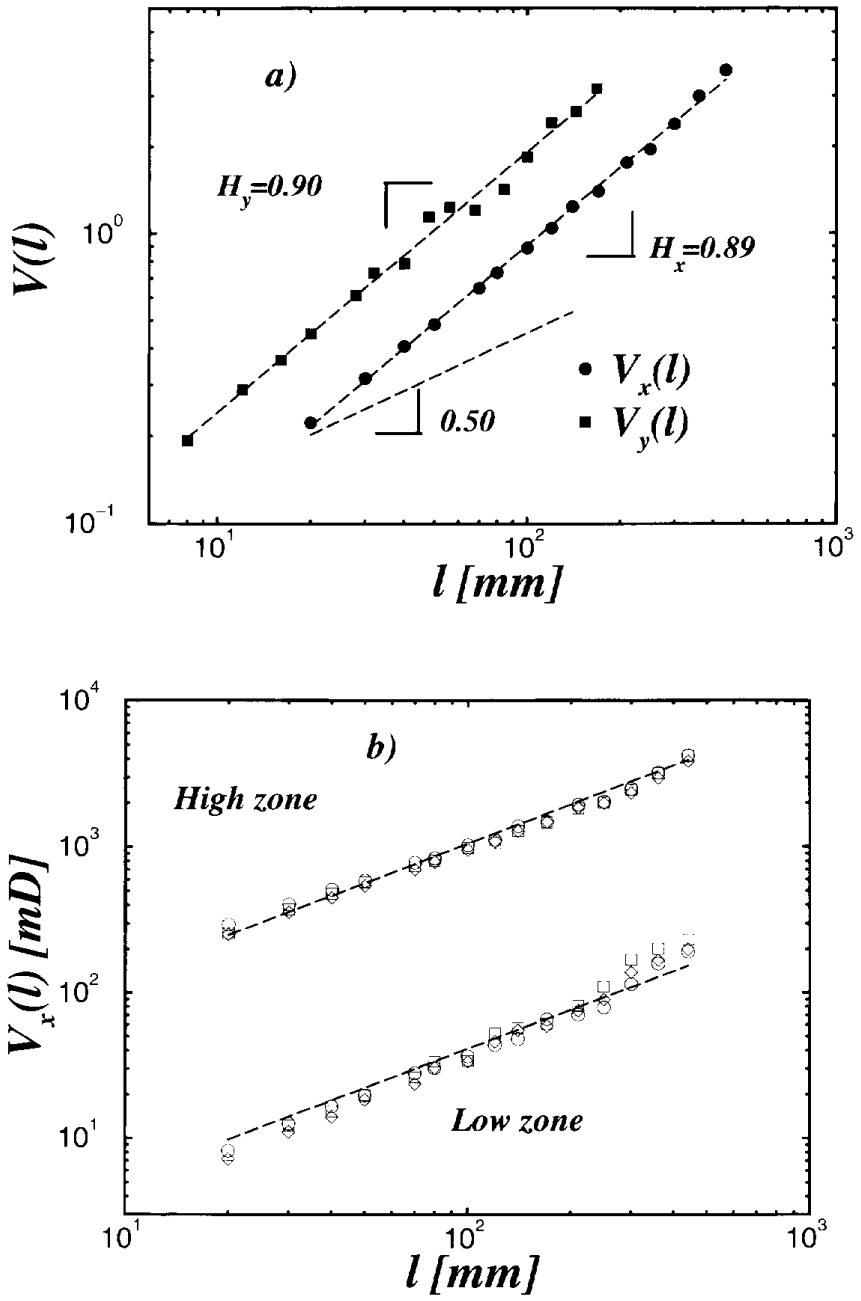

Fig. 4. Log–log plot of the variances of the permeability calculated using the DFA method for the sample Ho. (a) Variances $V_x(\ell)$ and $V_y(\ell)$ along the x and y directions, respectively, averaged over the three different faces of the sample, and averaged over the high and low permeability zones together for $V_x(\ell)$ and over the high permeability zone for $V_y(\ell)$. The power-law relationship between the variance and the separation distance ℓ is characterized by exponents $H_x = 0.89 \pm 0.06$ and $H_y = 0.90 \pm 0.06$. The exponents are the same within error bars indicating the isotropy of the correlations in the xy plane. (b) Variance $V_x(\ell)$ calculated along the x direction for the high and low permeability zones, separately. Data are averaged over the three different faces of the sample. Both set of data are consistent with a power law $H_x \simeq 0.89$, showing that the spatial correlations are the same in both zones.

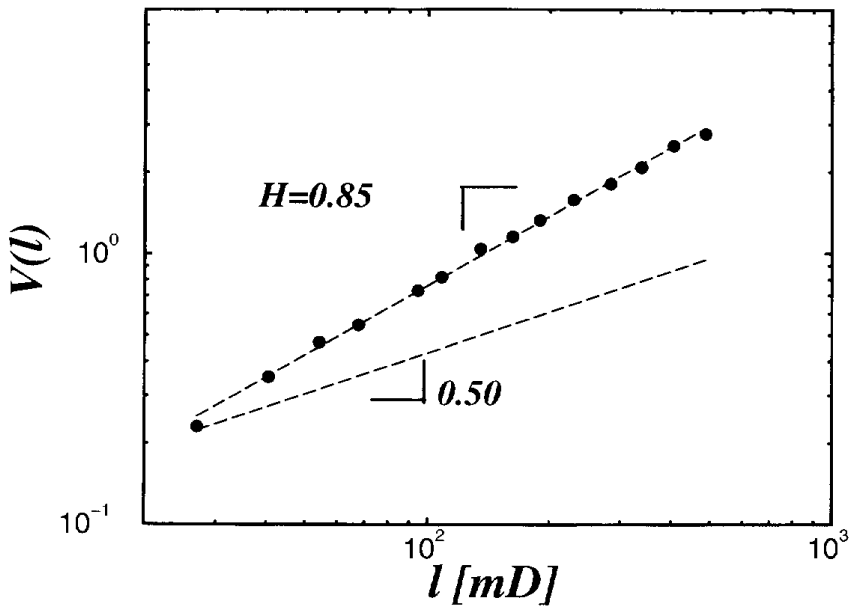

Fig. 5. Log–log plot of the variance calculated along the y' for the high permeability zone of Sample Lo, averaged over the three different faces of the sample. Along the y' direction, a correlation exponent of $H = 0.85 \pm 0.06$ is found. However, along the x' direction, a periodic pattern is observed. Thus, the anisotropy in this sample is manifested in a change of behavior from long-range correlation scaling along y' to periodic morphology along x'.

power law where $H_x \simeq 0.89$, independent of the magnitude of the overall permeability. These values are confirmed, within the error bars, using the wavelet analysis. We find that

$$H_x = 0.82 \pm 0.06, \qquad H_y = 0.84 \pm 0.06 \qquad \text{(Ho: Wavelet)}. \tag{9}$$

As seen in Fig. 1(a), the high permeability zone of sample Lo presents strong anisotropy with anisotropic axes (x', y') not coincident with the coordinate frame (x, y) (see Fig. 1(a)). We calculate the variance along the y' direction (parallel to the direction of the crests) and find (Fig. 5) using the DFA method

$$H_{y'} = 0.85 \pm 0.06 \qquad \text{(Lo: DFA)}, \tag{10}$$

a value that is consistent with our findings for the Sample Ho. Using wavelet analysis, we find

$$H_{y'} = 0.84 \pm 0.06 \qquad \text{(Lo: Wavelet)}. \tag{11}$$

Along the x' direction a periodic morphology is observed with a wavelength of about 60 mm. This introduces a characteristic length scale so that no scale invariance power law correlations are expected along this direction. The existence of this laminar periodic structure is consistent with a depositional model of sand dune dynamics [9].

Thus, for both methods we find that $H > \frac{1}{2}$, thereby demonstrating the presence of long-range correlations in the Ho and Lo samples.

6. Model

We incorporate the spatial correlation properties of real systems into the framework of the percolation problem [22], to investigate the effects that this has on the various quantities of interest, and to consider the consequent implications.

As an example, imagine an oil reservoir made from a river system. The old river channels represent good sand with high permeability. The other rock (shale) has poor permeability. Hence, for many purposes it can be modeled by a conductor/insulator or percolation system. The sand bodies may be thought of as some shapes distributed in space. They may tend to avoid each other or stack next to each other. Fortunately, for the petroleum industry, they may also overlap, so it is possible for large "clusters" of sand bodies to exist.

In order to quantify these ideas, we consider the *correlated* percolation model [23–26]. In the limit where correlations are so small as to be negligible a site in the square lattice is occupied *at random* with a probability p [22]. However, the fact that we find *spatial correlations* in the rock suggest that the process can be better modeled using the correlated percolation model where each site is not independently occupied, but is occupied with a probability that depends on the occupancy of the neighborhood. For a method of generating long-range correlations, see Section 7. We analyze the structural and dynamic properties of the resulting connected structure. It is worth noting that the percolation model applies not only to the scale of the pore structure but also to larger scales such as the lamination scale. For both the discrete (sand/shale) and continuous systems (permeability), it is important to know how long-range correlations influence the macroscopic connectivity and flow.

The impact of correlations is apparent from Fig. 6. Fig. 6(a) is for conventional uncorrelated percolation, and Fig. 6(b) is for percolation with long-range scale-invariant correlations. Both figures are plotted at the critical concentration p_c, above which fluid can flow since there exists an "incipient infinite cluster" that forms just when a connected path breaks through. The occupancy probability p corresponds to the net to gross or volume fraction of good sand in actual sand systems. It is apparent by visual inspection that the clustering properties for the two cases differ dramatically. For example, by comparing Figs. 6(a) and (b), we see that the clusters are much larger and more compact in the case of long-range correlations. This implies that there are fewer dead-ends and hence less unswept oil. Therefore, the recovery percentage increases for such strongly correlated systems. Our preliminary results indicate an increase of about 10% in the recovery percentage of correlated systems in comparison with uncorrelated systems.

Fig. 7 shows the changes with the correlation exponent γ of the fractal dimension of the minimum path, d_{min} (the shortest path that one can get through the cluster from one to the other). The correlation exponent γ measures the degree of correlation in the system, being uncorrelated for $\gamma = 2$ and strongly correlated for $\gamma = 0$. Again we see a striking dependence of this property upon the degree of correlations. The fractal dimension of the minimum path approaches one (the minimum path becomes equal to

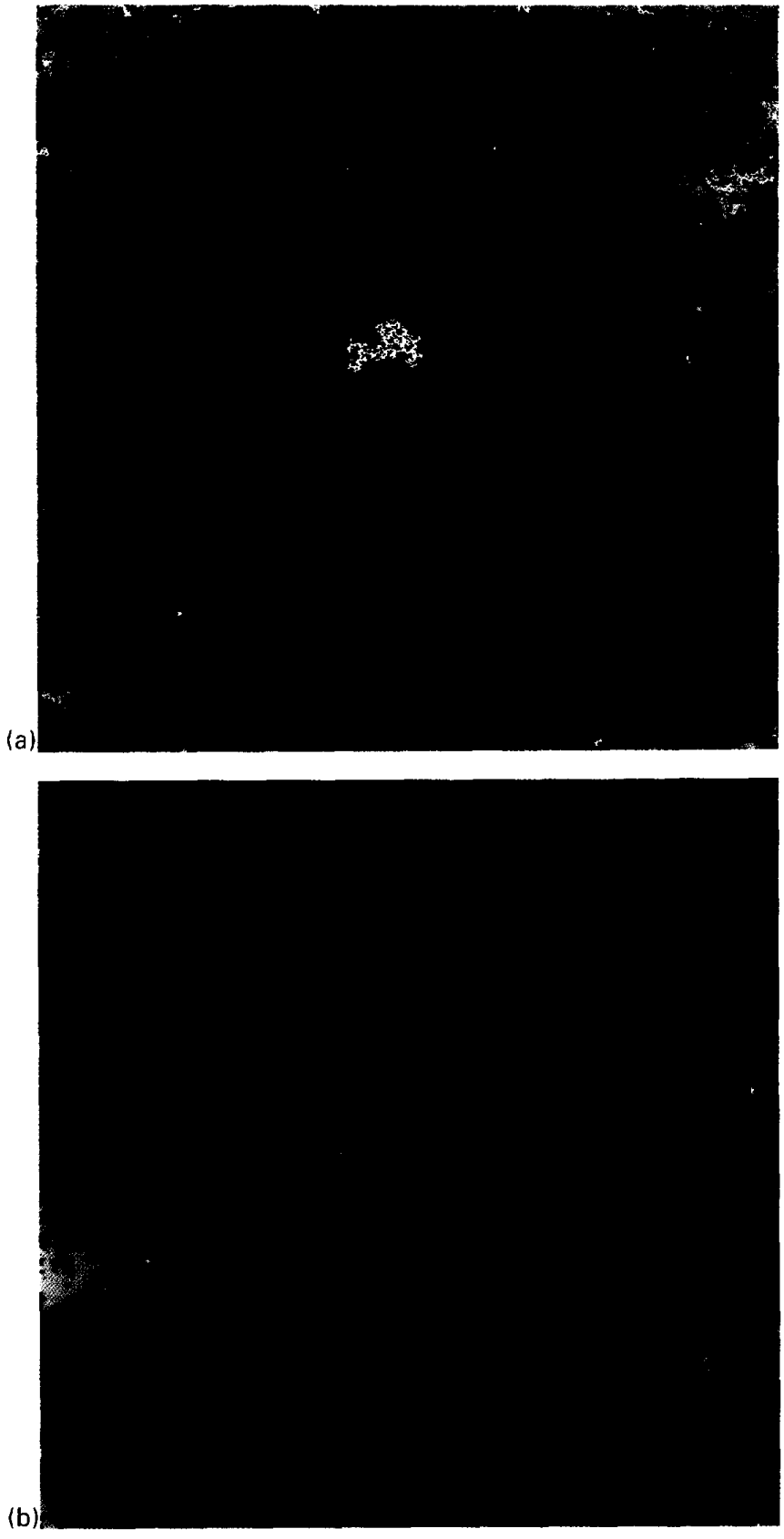

Fig. 6. Percolation at the critical concentration: (a) uncorrelated case, and (b) correlated case.

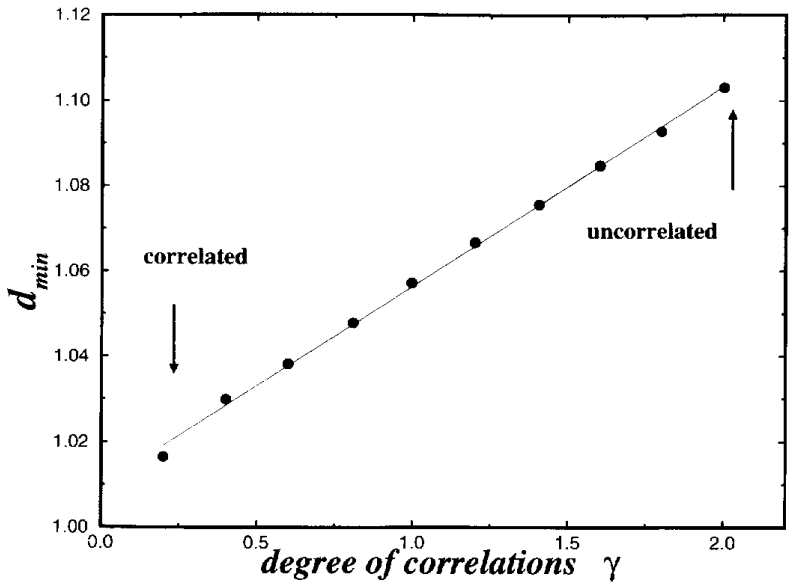

Fig. 7. Fractal dimension d_{min} as a function of the degree of correlations.

the Euclidean distance between the points) as $\gamma \to 0$ (strong correlations), meaning that the cluster becomes more compact in agreement with the above behavior. The fact that the shortest streamlines are "straighter" leads to shorter breakthrough times. As the tortuosity of the streamlines is reduced, we expect dispersion of the front to be reduced and hence better recovery efficiency.

Similar analyses have been performed with other quantities characterizing the connectivity properties of the percolation clusters. For example, we find that the critical concentration p_c increases as a function of γ. Therefore, one would expect better overall connectivity at lower net to gross in the correlated case than in the uncorrelated case. The quantitative changes with the degree of correlations indicate the errors that are being made with currently used uncorrelated models.

7. Method of generating long-range correlations

One of the most used methods to generate a sequence of random numbers with power-law correlations is the Fourier filtering method (Ffm) [25,27,28]. It consists of filtering the Fourier components of a uncorrelated sequence of random numbers with a suitable power-law filter in order to introduce correlations among the variables. This method has the disadvantage of presenting a finite cutoff in the range over which the variables are actually correlated [25,28]. Other methods present similar problems (see, for instance, Ch. 9 in Feder's book [27]). As a consequence, one must generate a very large sequence of numbers, and then use only the small fraction of them that are actually correlated (this fraction can be as small as 0.1% of the initial length of the sequence [25,28]). This limitation makes the Ffm not suitable for the study of scaling

properties in the limit of large systems.

Here we modify the Ffm in order to remove the cutoff in the range of correlations. We show that in the modified method the actual correlations extend to the *whole system* [29].

7.1. Conventional Fourier filtering method (Ffm)

We start by defining the Ffm for the $d = 1$ case (d is the dimension of the sample). Consider a stationary sequence of L uncorrelated random numbers $\{u_i\}_{i=1,\ldots,L}$. The correlation function is

$$\langle u_i u_{i+\ell} \rangle \sim \delta_{\ell,0}\,, \tag{12}$$

with $\delta_{\ell,0}$ the Kronecker delta, and the brackets denote an average with respect to a Gaussian distribution. The goal is to use the sequence $\{u_i\}$, in order to generate a new sequence, $\{\eta_i\}$, with a long-range power-law correlation function $C(\ell)$ of the form

$$C(\ell) \equiv \langle \eta_i \eta_{i+\ell} \rangle \sim \ell^{-\gamma} \qquad (\ell \to \infty)\,. \tag{13}$$

Here, γ is the correlation exponent, and the long-range correlations are relevant for $0 < \gamma < d$, where $d = 1$. The spectral density $S(q)$ defined as the Fourier transform of $C(\ell)$ has the asymptotic form

$$S(q) = \langle \eta_q \eta_{-q} \rangle \sim q^{\gamma - 1} \qquad (q \to 0)\,. \tag{14}$$

Here $\{\eta_q\}$ correspond to the Fourier transform coefficients of $\{\eta_j\}$, and satisfies

$$\eta_q = (S(q))^{1/2} u_q\,, \tag{15}$$

where $\{u_q\}$ are the Fourier transform coefficients of $\{u_i\}$.

The actual numerical algorithm for Ffm consists of the following steps:

(i) Generate a one-dimensional sequence $\{u_i\}$ of uncorrelated random numbers with a Gaussian distribution, and calculate the Fourier transform coefficients $\{u_q\}$. (In practice, one can generate directly $\{u_q\}$ from a sequence of uncorrelated random numbers.)

(ii) Obtain $\{\eta_q\}$ using (14) and (15).

(iii) Calculate the inverse Fourier transform of $\{\eta_q\}$ to obtain $\{\eta_i\}$, the sequence in real space with the desired power-law correlation function (13).

7.2. New method

The Ffm method has been applied in a number of studies of correlated systems [25,28]. However, an analysis of the method for large L shows that, by following the above procedure, one ends up with a sequence of correlated numbers whose range of correlations, for $d = 1$, is only about 0.1% of the system size. For example, from

an initial sequence of 10^6 numbers, only 10^3 numbers show the desired power-law correlations [28]. For $d = 2$, the range of correlations increases to 1% of the system size [25]. In order to remove this artificial cutoff in the correlations, we modify the Ffm algorithm as follows [29]:

(a) To calculate the spectral density $S(q)$, a well-defined correlation function in the real space is needed. The function $C(\ell) = \ell^{-\gamma}$ has a singularity at $\ell = 0$. We replace (13) with a slightly modified correlation function that has the desired power-law behavior for large ℓ, and is well-defined at the origin

$$C(\ell) \equiv (1 + \ell^2)^{-\gamma/2} . \tag{16}$$

(b) The relation (15) is based on the convolution theorem, and therefore the desired correlation function (16) must satisfy the proper periodic boundary condition. The function $C(\ell)$ can be naturally extended to negative values of ℓ due to the ℓ^2 dependence. We define (16) in the interval $[-L/2,\ldots,L/2]$, and impose periodic boundary conditions, i.e. $C(\ell) = C(\ell + L)$,

$$C(\ell) = \begin{cases} (1 + \ell^2)^{-\gamma/2} & \text{if } 0 \leqslant \ell \leqslant L/2 - 1, \\ (1 + (L - \ell)^2)^{-\gamma/2} & \text{if } L/2 \leqslant \ell < L. \end{cases} \tag{17}$$

(c) The discrete Fourier transform of (16) – needed to obtain η_q using (15) – can now be calculated analytically,

$$S(q) = \frac{2\pi^{1/2}}{\Gamma(\beta + 1)} \left(\frac{q}{2}\right)^{\beta} K_\beta(q) , \tag{18}$$

where q takes values $q = 2\pi m/L$ with $m = -L/2,\ldots,L/2$, $K_\beta(q)$ is the modified Bessel function of order $\beta = (\gamma - 1)/2$, and Γ is the gamma function.

The modified Bessel functions satisfy the asymptotic relations

$$K_\beta(q) = \begin{cases} \dfrac{\Gamma(\beta)}{2} \left(\dfrac{q}{2}\right)^{\beta} & \text{if } q \gg 1 , \\ \sqrt{\dfrac{\pi}{2q}} e^{-q} & \text{if } q \ll 1 , \end{cases} \tag{19}$$

for β positive and by definition $K_{-\beta} = K_\beta$. Then for small values of q, (18) gives the same asymptotic form as (14). However, the Bessel function introduces a cutoff for large q in the sense that $S(q)$ has a faster exponential decay. This cutoff, while irrelevant to the long-distance scaling, is very important for the validity of the whole Fourier analysis because it avoids aliasing effects (see [30, Ch. 7]). The cutoff in the Fourier space is thus responsible for eliminating the cutoff in real space observed in the Ffm method.

In order to perform the above steps numerically, we employ the Fast Fourier transform [30]. The calculation of the regular Fourier transform involves $O(L^2)$ operations. Using the fast Fourier transform algorithm the process is computed in $O(L \log L)$ operations, which gives a drastic difference in computing time, and makes this method

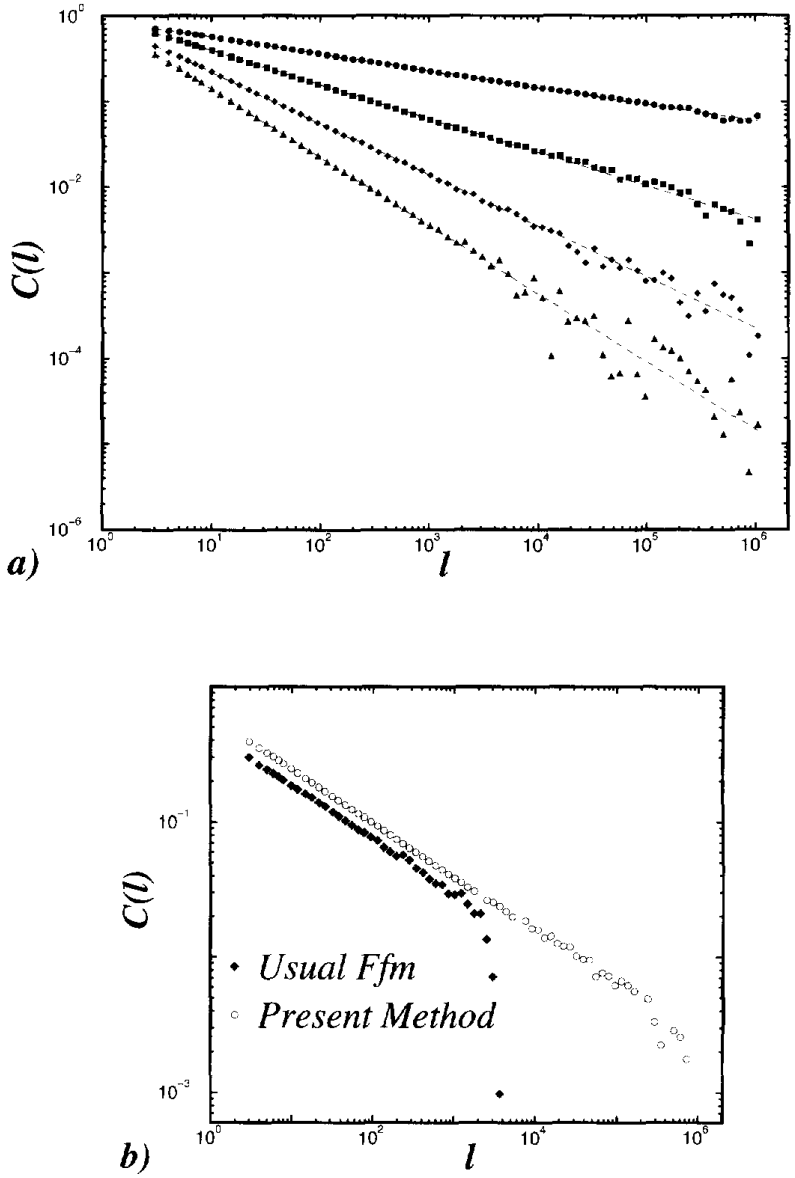

Fig. 8. (a) A log–log plot of the average correlation $C(\ell)$ of 50 correlated samples obtained with the proposed method for $L = 2^{21}$. Shown are results for different values of the desired $\gamma = 0.2, 0.4, 0.6$, and 0.8 (from top to bottom). The dashed lines represent the best fits which yield the nominal values of $\gamma = 0.19 \pm 0.02$, 0.39 ± 0.02, 0.60 ± 0.03 and 0.79 ± 0.03. The correlations are calculated until $L/2$ due to the periodic boundary conditions. (b) Comparison between the usual Ffm and the proposed method. We see how the correlations are extended until 0.1% of the system size in the case of the usual Ffm, while the correlations span all the system size when our method is used instead. In both cases we average over 50 samples; we use $L = 2^{21}$ and $\gamma = 0.4$.

very fast. Due to the periodic boundary condition imposed on the correlation function in (17), it follows that the correlated sample satisfies the same periodicity. If one requires a sequence with open boundary conditions, we generate twice as many numbers and then split the sequence into two parts. Another numerical detail that should be considered is that the correlation function in the Fourier space is not defined for $q = 0$.

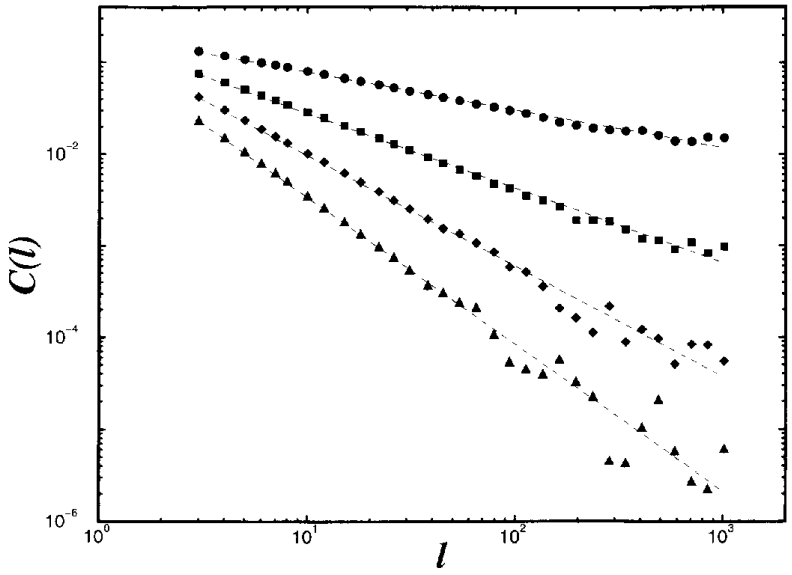

Fig. 9. Log–log plot of the correlations along the diagonal direction in a square lattice of $2^{11} \times 2^{11}$. Shown are results for different values of $\gamma = 0.4, 0.8, 1.2$ and 1.6 (from top to bottom), and we take averages over 50 samples. The fits yield nominal values of $\gamma = 0.41 \pm 0.02$, 0.81 ± 0.03, 1.20 ± 0.03 and 1.59 ± 0.04.

This comes from the fact that we are using a continuum limit to calculate the Fourier transform instead of the discrete definition. However, the zero frequency only adds an additive constant to the numbers, and does not affect the scaling properties of the sequence. This singularity can be avoided anyway, by assigning a suitable numerical value $0 < m_0 < 1$ instead of $m = 0$.

To test the actual correlations of the generated sample $\{\eta_i\}$ we calculate $C(\ell)$ averaging over different realizations of random numbers. Fig. 8(a) shows a plot of the actual correlations obtained for different values of γ and for a sequence of $L = 2^{21}$ numbers. It is seen that the long-range correlations exist for the *whole* system. The nominal values of γ obtained from the best fits are also the same, within the error bars, as the desired input values. In Fig. 8(b), we compare the proposed method with the usual Fourier filtering method.

To summarize the method, the correlation function we propose is well-defined and satisfies the correct power-law behavior in real space. Its Fourier transform has the correct power law at small frequencies, and presents a cutoff for large frequencies that avoids aliasing effects, and leads to the infinite long-range behavior in real space.

7.3. *Generating long-range correlations in d dimensions*

The algorithm can be easily generalized to higher dimensions. In a d-dimensional cube of volume L^d the desired correlation function takes the form

$$C(\underline{\ell}) = \left(1 + \sum_{i=1}^{d} \ell_i^2\right)^{-\gamma/2}, \tag{20}$$

with the corresponding periodic boundary condition, $C(\underline{\ell}) = C(\underline{\ell} + \underline{L})$. The spectral density is

$$S(\underline{q}) = \frac{2\pi^{d/2}}{\Gamma(\beta_d + 1)} \left(\frac{q}{2}\right)^{\beta_d} K_{\beta_d}(q), \tag{21}$$

where $q = |\underline{q}|$, $q_i = 2\pi m_i/L$, $-L/2 \leqslant m_i \leqslant L/2$, $i = 1, \ldots, d$, and $\beta_d = (\gamma - d)/2$. In the two-dimensional case the correlated variables are defined in a (x, y) square lattice $\{\eta_{i,j}\}$. Fig. 9 shows a test of the actual correlations obtained in two dimensions for different degree of correlations, and for a system of lateral size $L = 2^{11}$.

8. Conclusions

Spatial patterns in permeable rocks exist and require quantitative methods to describe them. In the particular case of Aeolian systems (such as the Lochabriggs sample), we show that the observed periodic stratified pattern can be understood with a "table-top" experiment. We propose a physical explanation for the formation of layers, which is related to a size segregation effect and also to the existence of *two* critical angles controlling the avalanche process. Finally, we develop a stochastic model of sand dune dynamics that confirms the plausibility of this physical mechanism. While these results apply only to aeolian systems, the finding of long-range correlations in sandstone appears to be true independent of the geological process involved. For the two samples studied so far it has been shown that the correlations can be well modeled using a power law.

These spatial patterns have very great consequences for prediction of, for example, hydrocarbon recovery or contaminant transport in ground water. The fact that there exist long-range correlations implies that contaminant transport might be less dispersed than would be predicted from a short range correlation model.

Acknowledgements

We thank P. Cizeau, R. Cuerno, G. Davies, P.-G. de Gennes, D. Langtry, and S. Tomassone for discussions and BP for financial support.

References

[1] R.A. Bagnold, The Physics of Blown Sand and Desert Dunes (Chapman and Hall, London, 1941).
[2] E.D. McKee, E.J. Crosby and H.L. Berryhill, J. Sedimentary Petrol. 37 (1967) 829–851.
[3] A.V. Jopling and R.G. Walker, J. Sedimentary Petrol. 38 (1968) 971–984.
[4] J.L. Borges, The Book of Sand (Emecé, Buenos Aires, 1975).
[5] S.G. Fryberger and C. Schenk, Sedimentology 28 (1981) 805–821.
[6] R.J. Cheel and G.V. Middleton, J. Geology 94 (1986) 489–504.
[7] R.E. Hunter, J. Sed. Petrol. 55 (1985) 886.
[8] S.G. Buck, J. Sed. Petrol. 55 (1985) 895.

[9] H.A. Makse, S. Havlin, P.R. King and H.E. Stanley, Nature (submitted).
[10] H.S. Hele-Shaw, Nature 58 (1898) 34–36.
[11] R.A. Bagnold, Proc. Roy. Soc. London A 295 (1966) 219–232.
[12] J.R.L. Allen, J. Geology 78 (1970) 326–351.
[13] H.M. Jaeger and S.R. Nagel, Science 255 (1992) 1523–1531.
[14] H.A. Makse, G. Davies, S. Havlin, P.Ch. Ivanov, P.R. King and H.E. Stanley, Phys. Rev. E 54 (October 1st, 1996).
[15] C. Halvorsen and A. Hurst, in: Advances in Core Evaluation Accuracy and Prediction, eds. P.F. Worthington (Gordon and Breach, London, 1990).
[16] The spatial average over a window of size ℓ is denoted by the overbar, and the disorder average over different displacements (x_j and y_i) is denoted by the angular brackets.
[17] T. Vicsek, Fractal Growth Phenomena, 2nd ed., Part IV (World Scientific, Singapore, 1992); J. Kertész and T. Vicsek, in: Fractals in Science, eds. A. Bunde and S. Havlin (Springer, Heidelberg, 1994); P. Meakin, Phys. Rep. 235 (1993) 189; T. Halpin-Healey and Y.-C. Zhang, Phys. Rep. 254 (1995) 215; A.-L. Barabasi and H.E. Stanley, Fractal Concepts in Surface Growth (Cambridge Univ. Press, Cambridge, 1995); F. Family and T. Vicsek, eds., Dynamics of Fractal Surfaces (World Scientific, Singapore, 1991).
[18] The exponent H is called the Hurst exponent for the associated fractional Brownian motions (fBm) $x_j(\ell)$ and $y_i(\ell)$ defined by Eq. (5). However, we must note that the original permeability $k(i,j)$ is fractional Gaussian noise (fGn). Therefore, in a numerical study of the effect of long-range correlations in porous media, we must generate the permeability values from a fGn and not from a fBm.
[19] C.K. Peng, S.V. Buldyrev, S. Havlin, M. Simons, H.E. Stanley and A.L. Goldberger, Phys. Rev. E 49 (1994) 1685–1689.
[20] H. Leschhorn and L.-H. Tang, Phys. Rev. Lett. 70 (1993) 2973; H.A. Makse and L.A.N. Amaral, Europhys. Lett. 31 (1995) 379.
[21] J.F. Muzy, E. Bacry and A. Arneodo, Phys. Rev. Lett. 67 (1991) 3515; A. Arneodo, E. Bacry, P.V. Graves and J.F. Muzy, ibid 74 (1995) 3292.
[22] A. Bunde and S. Havlin, eds., Fractals in Science (Springer, Berlin, 1994).
[23] A. Coniglio, C. Nappi, L. Russo and F. Peruggi, J. Phys. A 10 (1977) 205–209.
[24] A. Weinrib, Phys. Rev. B 29 (1984) 387–395.
[25] S. Prakash, S. Havlin, M. Schwartz and H.E. Stanley, Phys. Rev E 46 (1992) R1724.
[26] H.A. Makse, S. Havlin, H.E. Stanley and M. Schwartz (1993 Int. Conf. Complex Systems in Computational Physics, Buenos Aires) Chaos, Solitons and Fractals 6 (1995) 295.
[27] D. Saupe, in: The Science of Fractal Images, eds. H.-O. Peitgen and D. Saupe (Springer, New York, 1988); J. Feder, Fractals (Plenum Press, New York, 1988).
[28] C.K. Peng, S. Havlin, M. Schwartz and H.E. Stanley, Phys. Rev. A 44 (1991) 2239.
[29] H.A. Makse, S. Havlin, M. Schwartz and H.E. Stanley, Phys. Rev. E 53 (1995) 5445.
[30] W.H. Press, S.A. Teukolsky, W.T. Vetterling and B.P. Flannery, Numerical Recipes in Fortran, 2nd ed. (Cambridge Univ. Press, Cambridge, 1992).